PAPER

Check for updates

Detecting structural transformation of cobalt phosphonate to active bifunctional catalysts for electrochemical water-splitting†

Arindam Indra, [ID] [ab] Prashanth W. Menezes, [ID] *[b] Ivelina Zaharieva,[c] Holger Dau [ID] *[c] and Matthias Driess [ID] *[b]

In recent years, several cobalt-based catalysts have been developed for water splitting because of their promising activity, stability and structural motifs. Here, we report that cobalt phosphonate represents a novel class of bifunctional single-source precursors for highly efficient alkaline electrochemical O_2 evolution (OER) and H_2 evolution reaction (HER). Inspired by its favorable catalytic OER and HER activity, an overall water-splitting device has been constructed from this precursor, showing very low cell voltage (1.62 V @ 10 mA cm^{-2}) and excellent long-term stability. Depending on the applied oxidation and reduction potential on cobalt phosphonate, two distinct modified structures at the anode and cathode have been uncovered employing the *quasi in situ* X-ray absorption spectroscopy and *ex situ* methods. During OER, the phosphonate precursor reorganized itself to layered $CoO_x(OH)_y$ structure with defects and disorders, while the contribution of the metallic Co along with Co_3O_4 spinel and $Co(OH)_2$ is evident to drive the HER. The presented work demonstrates the advantage of using the 'all-in-one' precursor approach to realize bifunctional water-splitting electrocatalysts through the evolution of different species with self-supporting interfacial structural features at the anode and cathode during electrochemical water splitting.

Introduction

Electrochemical energy conversion by splitting water into O_2 and H_2 may become pivotal in providing clean and sustainable energy replacing fossil fuels.[1–3] The water-splitting process comprises of two half-cell reactions-oxygen evolution reaction (OER) at the anode and hydrogen evolution reaction (HER) at the cathode.[4–6] Water splitting is a thermodynamically uphill reaction and electrolysis of water requires a huge amount of energy in terms of potential.[5] Moreover, the O–O bond formation during OER requires the removal of four electrons and four protons from two water molecules involving high-energy intermediates.[7] Therefore, special attention has been provided to develop an efficient catalyst system for the overall water splitting reactions.[8]

Although noble metal-based RuO_2 and IrO_2 catalysts produce high water oxidation activity and Pt is known for the excellent hydrogen evolution, scarcity and cost of these materials limit their use for large-scale applications.[9,10] Recently, first-row transition metal-based catalysts have been widely explored for the OER and HER.[11–13] In this respect, cobalt-based materials are of particular importance because of their promising water-oxidation activity at reasonable overpotentials and regarding the understanding of structural and functional properties during water oxidation.[14–17] After the first report of *in situ* generated cobalt (oxide) phosphate (CoPi) catalyst for the efficient oxygen evolution in the neutral medium by Nocera and co-workers,[18,19] several crystalline and amorphous cobalt phosphates and oxides have extensively been investigated for electrocatalytic OER.[16,20–24] Most of the cobalt-based catalysts produce high electrochemical water oxidation activity in the alkaline medium through the activation of the catalyst into amorphous cobalt hydroxide–oxyhydroxide.[16,25–27] In many cases, the transformation is limited to the surface of the particles to form an amorphous shell while complete amorphization of the particles has been observed for the ultra-small nanoparticles.[24,26] Reversible amorphization of the catalytic species in cobalt oxide has also been demonstrated by some of us.[15] Moreover, the coordination environment around the cobalt center and the local structure has also shown to control the OER activity.[22,28]

[a]Department of Chemistry, Indian Institute of Technology (BHU), Varanasi, Uttar Pradesh-221005, India

[b]Department of Chemistry: Metalorganics and Inorganic Materials, Technische Universität Berlin, Straße des 17 Juni 135, Sekr. C2, 10623 Berlin, Germany. E-mail: prashanth.menezes@mailbox.tu-berlin.de; matthias.driess@tu-berlin.de

[c]Fachbereich Physik, Freie Universität Berlin, Arnimallee 14, 14195 Berlin, Germany. E-mail: holger.dau@fu-berlin.de

† Electronic supplementary information (ESI) available: Characterization of the catalysts by spectroscopic, microscopic, PXRD and analytical techniques along with the details of the experimental and electrochemical techniques. See DOI: 10.1039/c9ta09775a

This journal is © The Royal Society of Chemistry 2020

J. Mater. Chem. A, 2020, **8**, 2637–2643 | **2637**

On the other hand, the structural transformation of the cobalt-based catalyst during electrochemical HER has mostly been investigated only by *ex situ* methods.[16,29–31] The *ex situ* methods have various drawbacks including the oxidation of the precatalysts in alkaline conditions and the possible surface oxidation of the active phase in aerial conditions.[5] Therefore, it is highly desirable to investigate the active catalyst structure through *in situ* methods.

Though a series of cobalt (oxide) phosphate-based catalysts have been explored for the OER[16,20–24,26,27] and HER,[16,29,30,32–34] their use for the overall water splitting is fostered in the last few years. Cobo *et al.* have developed a Janus cobalt-based catalyst for the OER and HER at neutral pH.[35] The catalyst showed the formation of metallic Co coated with a cobalt-oxo/hydroxophosphate during HER in neutral medium.[35] Recently, we reported helical cobalt borophosphates for the electrochemical water splitting in the alkaline medium where the structural transformation of the catalyst at the anode and cathode was observed to attain two different active catalyst structures.[36] Therefore, understanding the structural transformation and realizing the structure of such active catalysts for both HER and OER is of fundamental interest to establish the structure–activity correlation.

Here we report a new class of material: cobalt phosphonate (CoPn) for electrochemical water splitting in alkaline medium. Phosphonates coordinate to the metal ion through the oxygen atoms and the reaction conditions significantly affect the local environment of the coordination around the metal centers (Fig. S1†).[37] Though these inorganic–organic hybrid materials are known for a long time, their applications for the photochemical and electrochemical water oxidation have been explored only recently.[38–42] Inspired by the excellent photochemical as well as electrochemical water oxidation of the phosphonates,[38–42] we have prepared CoPn and employed for the unification of electrochemical water oxidation, proton reduction, and overall water splitting. The nickel foam (NF) supported CoPn produced excellent OER activity in an alkaline medium to reach the current density of 10 mA cm^{-2} at only 240 mV overpotential whereas an overpotential of 144 mV was required for HER to attain the same current density. In addition, the designed alkaline overall water-splitting device displayed a cell voltage of only 1.62 V to reach the current density 10 mA cm^{-2}, making it one of the promising materials towards efficient water splitting. Further, the structural insights gathered from *quasi in situ* and *ex situ* experiments revealed that with applied potential CoPn transformed into a layered Co oxide structure, related to the crystalline LiCoO$_2$ or crystalline CoO(OH) but with clearly lower degree of order during OER whereas the HER catalyst comprises of metallic cobalt, Co$_3$O$_4$ and Co(OH)$_2$.

Results and discussion

CoPn was synthesized by the solvothermal reaction of Co(NO$_3$)$_2$·6H$_2$O and diethylenetriamine penta(methylenephosphonic acid) [DTPMP] (see the details in Experimental in ESI†). The material was purely amorphous in nature as revealed by the powder X-ray diffraction (Fig. S2†). Infrared spectrum detects the corresponding vibrations related to CoPn, as discussed in detail in the ESI (Fig. S3†).[43] The amorphous structure of the particles was clearly visible by the transmission electron microscopic (TEM) studies (Fig. 1). High-resolution TEM could not detect any lattices, whereas the selected area diffraction pattern (SAED) also revealed the amorphous nature of the CoPn particles (Fig. 1). Energy dispersive X-ray (EDX) detects the presence of Co, N, and P in fresh CoPn (Fig. S4†). The elemental analysis reveals that the ratio C/N ~2.83 in CoPn (close to the theoretical value of C/N = 9/3 = 3).

The surface properties, oxidation state and surface composition of CoPn were analyzed by X-ray photoelectron spectroscopic (XPS) studies (Fig. S5†). In Co 2p XPS, two peaks corresponding to Co 2p$_{1/2}$ and Co 2p$_{3/2}$ appeared at the binding energies of ~797 eV and ~781 eV, respectively (Fig. S5a†). The spin–orbit coupling spacing value (2p$_{3/2}$–2p$_{1/2}$) of 15.96 eV indicates Co^{II} as the dominant species.[14,15] The O 1s signal of pristine CoPn showed two peaks (531.2 eV and 532.0 eV) corresponding to P–O–Co linkages and oxygen from water (Fig. S5b†).[43] The N 1s peak can also be deconvoluted into two peaks at 399.9 eV and 401.8 eV indicating the C–N-containing moiety and quarternary N (Fig. S5c†).[43] The P 2p peaks at binding energy 133.4 eV (2p$_{3/2}$) and 134.3 eV (2p$_{3/2}$) indicate the presence of PO$_x$ unit in the phosphonate and clearly matched with the literature reports (Fig. S5d†).[43]

The as-prepared CoPn was first deposited on nickel foam (NF) by electrophoretic deposition (EPD) and electrochemical performances were investigated in 1 M aqueous KOH solution by a typical three-electrode system. For comparison, the OER properties of bare NF and commercially available benchmark electrocatalysts were also studied under the same condition. As presented in Fig. 2a, CoPn/NF exhibited an excellent OER activity with an overpotential of 240 mV to drive geometrical catalytic current density of 10 mA cm^{-2} (330 mV at 100 mA cm^{-2}). The potential is significantly lower than noble metal catalysts RuO$_2$/NF, IrO$_2$/NF, and NF. Interestingly, the achieved current density and overpotentials for CoPn was also found to be comparable to recently reported NF supported transition metal catalysts (Table S1†).[44–46]
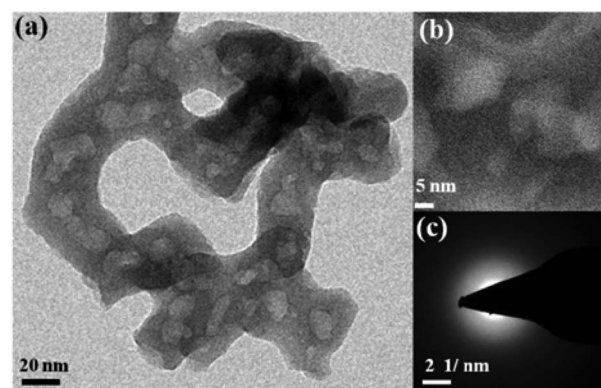

Fig. 1 (a) TEM image of CoPn, (b) high-resolution TEM image of CoPn and (c) electron diffraction pattern representing the amorphous nature of the material.
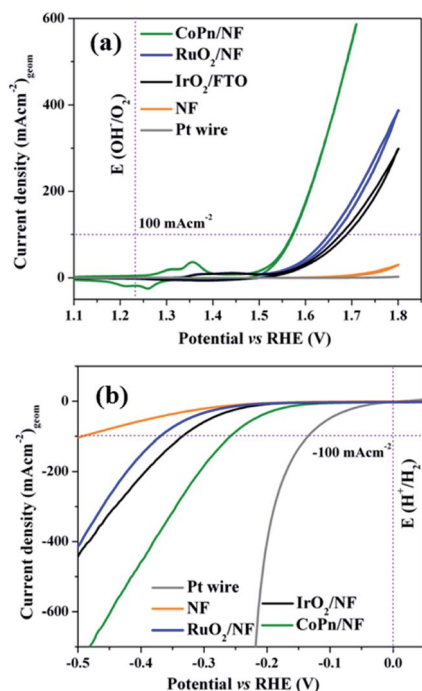
2638 | *J. Mater. Chem. A*, 2020, **8**, 2637–2643

This journal is © The Royal Society of Chemistry 2020

Fig. 2 (a) CV of OER and (b) LSV of HER for CoPn/NF and commercial noble metal-based catalysts in 1 M aqueous KOH at a scan rate of 1 mV s^{-1}.

To further illustrate the superior catalytic performance, the electrochemical impedance spectroscopy (EIS) was conducted where the Nyquist plots revealed very low charge-transfer resistance (R_{ct}) for CoPn/NF suggesting faster electron transfer rate between the interface of the catalyst that contributes to the higher OER activity (Fig. S6†).[47] The electrochemical double-layer capacitance (C_{dl}) was determined by cyclic voltammetry (CV) in the non-faradaic reaction range (Fig. S9†). A C_{dl} of 2.14 mF cm^{-2} was achieved for CoPn/NF that was almost thrice larger compared to bare NF (0.8 mF cm^{-2}).[48] The C_{dl} was then converted into ECSA using the specific capacitance (C_s) of the material per unit area ($C_s = 1.7$ mF cm^{-2} for NF),[47] and a value of 1.25 cm^2 (for details see Fig. S7† and Experimental section) was estimated for CoPn/NF demonstrating the presence of rich catalytically active sites than that of NF (0.47 cm^2).[49]

Two redox peaks were detected while cycling CoPn/NF between the potential values of 1.15 V and 1.45 V *vs.* RHE (Fig. S8†). These two peaks represent the oxidation of Co^{II} to Co^{III} and Co^{IV} during the electrochemical process to form active OER catalyst CoO$_x$(OH)$_y$.[50] The confirmation of the increase in the oxidation state was further proved by the *ex situ* XPS and *quasi in situ* X-ray absorption spectroscopic (XAS) studies (see later). Tafel plots assessed the catalytic reaction kinetics of CoPn/NF, and a slope of close to 60 mV (*ca.* 68 mV dec^{-1}) indicates that the OER mechanism proceeds through reversible electron transfer before reaching the turnover-limiting step (Fig. S9†).[51] Moreover, the excellent stability of the system has been achieved to show constant current production for more than 25 h under chronoamperometric (CA) conditions (Fig. S10†). A careful investigation of the CA profile reveals that

there was a significant increment in the current density within the first 12 h. The initial increase in the current density can be explained by the activation of the precatalyst (CoPn) to form the active water oxidation catalyst. As the transformation of the precatalyst to active catalyst was completed, a slight drop in current density was observed, indicating slow deactivation of the catalyst on longer run.

Similarly, the NF supported CoPn has been tested for HER in 1 M aqueous KOH solution. Only 144 mV of overpotential was required to achieve a current density of 10 mA cm^{-2} (Fig. 2b). Similar to OER catalysis, the catalytic HER performance of CoPn is better than the noble metal-based catalysts and bare NF but inferior to Pt. The activity of CoPn is also comparable to recently reported transition metal-based catalysts (Table S2†). A constant current was recorded to produce H$_2$ over 25 h under chronoamperometric conditions (Fig. S11†).

As most of the cobalt-based transition metal catalysts are transformed into CoO$_x$(OH)$_y$ during OER in alkaline medium,[26,31,36,50] we have extensively carried out studies on the structural transformation of CoPn. First, the catalyst was characterized by *ex situ* spectroscopic, microscopic and analytical methods after 25 h CA measurements. Destruction of the structure of the CoPn was detected by TEM studies (Fig. 3). A layered structure with overlapping plates was formed after the OER (Fig. 3a and b). The rings of the SAED could be attributed to the (110) and (130) planes of the Co(O)OH (JCPDF: 26-480). Similarly, CoPn also underwent complete transformation after HER-CA displaying rings of (220) (311) and (511) corresponding to the spinel Co$_3$O$_4$ phase (JCPDF: 42-1467) (Fig. 3c and d).

The XPS studies revealed that the oxidation state of Co was increased after the oxygen evolution (Fig. 4 and S12†). From the literature, it is well known that Co^{II} and Co^{III} ions have almost similar 2p binding energies (BE) but can be differentiated by the
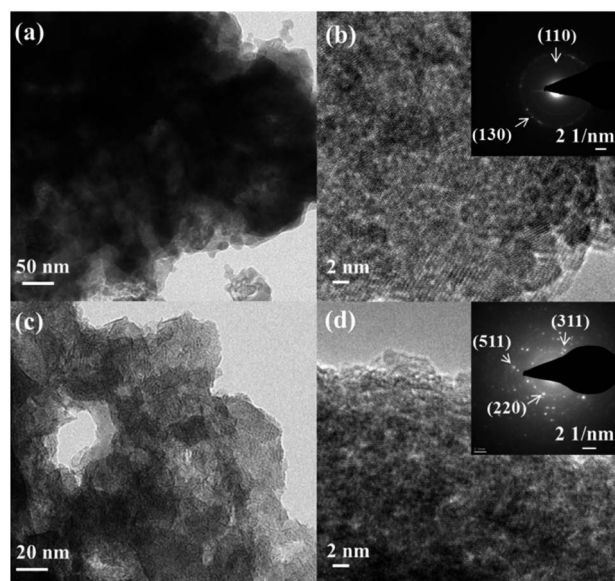

Fig. 3 TEM and HR-TEM images of CoPn after chronoamperometric OER (a and b) and HER (c and d) studies in 1 M alkaline KOH solution. The corresponding electron diffraction pattern is shown in the inset.
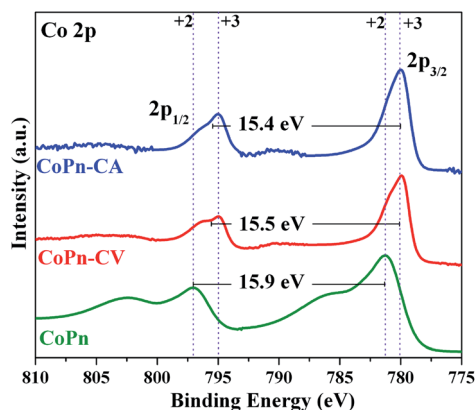
This journal is © The Royal Society of Chemistry 2020

J. Mater. Chem. A, 2020, **8**, 2637–2643 | **2639**

Fig. 4 Comparison of the Co 2p XPS spectra in pristine form and after OER-CV and OER-CA. As the binding energies of Co^{II} and Co^{III} sites are not unambiguous, they can be further differentiated by the Co $2p_{1/2}$–$2p_{3/2}$ spin−orbit level energy spacing. The difference of 16.0 eV represents high-spin Co^{II} whereas 15.0 eV comprises low-spin Co^{III}. The oxidation of Co^{II} to Co^{II} during OER is reflected in the decreased spin−orbit coupling values.

Co $2p_{1/2}$–$2p_{3/2}$ spin−orbit coupling value, which is 16 eV for high-spin Co^{II} and 15 eV for low spin Co^{III}.[17] An energy spacing of 15.5 eV was attained after OER CV that indicated the presence of mixed-valent Co^{II}–Co^{III} species. Moreover, after OER CA, the energy spacing was further reduced to 15.5 eV, which clearly confirmed the dominant amount of Co^{III} species.[17] The deconvolution of the Co 2p peaks also indicates the oxidation of Co^{II} to Co^{III} during the electrochemical process.[36] After the electrochemical measurements (both CV and CA), the O 1s peak was deconvoluted into three peaks. As anticipated, the peak corresponding to P–O–Co species was disappeared with the formation of the new peak for Co–O bonds (529.5 eV) from Co-oxide/hydroxide species (Fig. S13†).[26,50] The other two deconvoluted peaks of O 1s indicate substantial hydration (532.7–533.6 eV) and hydroxylation (531.4 eV) of the catalyst surface during electrochemical OER.[26,50] The signals from N and P in pristine CoPn were also disappeared after alkaline water oxidation (Fig. S14 and S15†). More detailed descriptions of the deconvoluted spectra are given in Fig. S12 to S15 of ESI.†

Similarly, the catalyst at the cathode was also characterized after HER CV and CA by XPS. The Co $2p_{1/2}$–$2p_{3/2}$ spin−orbit coupling value was calculated to be 15.5 eV after HER CV and 15.4 eV after CA, showing the formation of mixed valent Co^{II}–Co^{III} species (Fig. S16†).[36] The structural transformation of CoPn during HER was further confirmed from the O 1s spectra where the P–O–Co bridge was not detected. Instead, a new peak appeared at 529.5 eV for Co–O bonds (Fig. S17†).[36] Like in the case of OER, a significant amount of hydration (532.5 eV and 533.6 eV) of the catalyst was detected after HER.[14,24,31] The signal from P was also absent after HER confirming severe structural transformation at the cathode (Fig. S18†).[24] From XPS, it was clear that CoPn acts as the precatalyst and completely transformed into a combination of distinct active structures at the cathode and anode during electrochemical water splitting. Moreover, the transformation occurred within the first CV

measurement where a loss of over 90% phosphorous was attained, which is confirmed by the ICP-AES studies.

To have a more conclusive understanding of the structural transformation of CoPn during water oxidation with varying potential (CV) and at a constant potential (CA) *quasi in situ* Co K edge, X-ray absorption near edge spectroscopic (XANES) studies were carried out (Fig. 5). The XANES edge shape clearly revealed the structure of as-prepared CoPn remains intact even after EPD on the electrode, which is also consistent with the EXAFS spectra (Fig. S19 and Table S3†). After cycling (CV) and at CA relevant to OER, pronounced structural transformations were attained. The transformation was fast, and the structure of the catalyst after CV or CA at OER potentials was virtually the same (Fig. 4). The edge shape after OER resembles the one from amorphous layered oxides (CoCat) electrodeposited by Nocera's group (Fig. S20†).[27,52] This converted structure can be derived from the $LiCoO_2$ crystal structure, but in the present case, as well as in the catalysts from the group of Nocera, the edge was rather smooth and non-structured, a clear indication of the disordered structure of the catalyst. The simulation of the edge shape as a linear combination of spectra was difficult due to the amorphous character of the CoCat (lack of a well-defined crystal structure) and due to the known redox-activity of the Co ions in the structure, which does affect the edge position (the edge position will depend on the history of the applied potential).

To draw a further conclusion on the structure of the catalyst at OER potentials, we performed EXAFS simulations (Fig. 6 and S21†). First, we used an unbiased simulation approach to identify possible structures besides the layered CoCat of Nocera type. Evidence for the presence of other structures was ascertained by the appearance of the shoulder at the right side of the second FT peak (Fig. 6). This first simulation approach (Table S4†) indicated the possible presence of a spinel structure in the catalyst. To determine the percentage of the spinel structure, we repeated the simulation assuming a combination of ideal, crystalline spinel and ideal layered Co oxide (simulation approach 2 in Table S4†). The results suggested that there is about 20% of spinel structure in the OER catalysts.
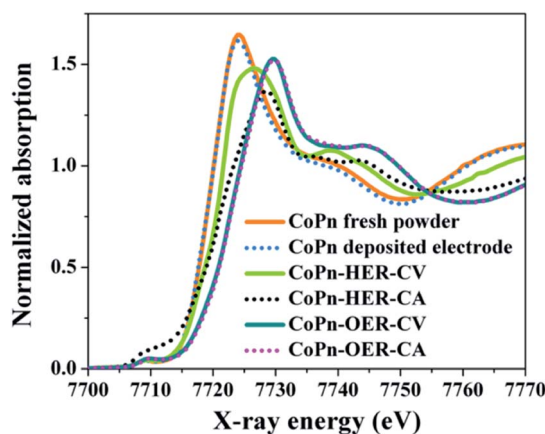

Fig. 5 *In situ* XANES Co K-edge spectra are showing the change in the oxidation state of Co from fresh CoPn during alkaline OER and HER at a constant potential (CA) as well as varying potential (CV).
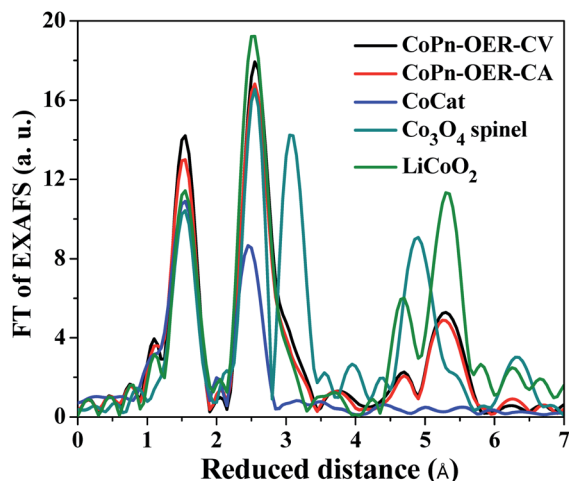
2640 | *J. Mater. Chem. A*, 2020, **8**, 2637–2643

This journal is © The Royal Society of Chemistry 2020

Fig. 6 FT of EXAFS of CoPn exposed to OER potentials compared with other catalysts. Two approaches to simulations are shown in Table S4.† Please note that $LiCoO_2$ is isostructural to CoOOH resulting in indistinguishable EXAFS spectra.

In the case of HER, the edge shape significantly changed (Fig. 4) after both CV and CA. The transformation was much slower after CV, and the changes were more pronounced after CA. To understand how these changes related to structural transformation, we simulated the edge spectra after CV and CA as a linear combination of edge spectra of some reference compounds (Fig. S22†). The results show that in both cases, the starting compound is destroyed. The spectrum after CV (Fig. S22a†) can be modeled as a linear combination of 38% hydrated Co^{2+} ions and 62% Co spinel structure (Co_3O_4). The spectrum after CA can be described as a linear combination of 4% Co^{2+} ions, 91% Co spinel structure, and 5% contribution from a metallic Co (Fig. S22b†). In our previous report with cobalt borophosphates,[36] we also detected the formation of Co^0 during HER, where favorable adsorption of water and proton on cobalt surface as well as the facile desorption of the intermediates from the surface was ascribed to be the reason for the enhancement in HER activity.[53,54] In fact, the local environment around the Co^0 plays a major role in controlling the Gibbs free energy of adsorption. For example, in the Janus H_2-Cat, Co^0 species encapsulated in the $Co(OH)_2$ shell provides the active sites for HER, while the N-doped carbon significantly lowers the adsorption free energy in Co@NC.[35,53,54] Therefore, in the present case, we propose the participation of Co^0 along with $Co(OH)_2/Co_3O_4$ species are responsible for the efficient alkaline HER.

This edge-shape simulation, especially, in the case of the catalyst after CA is not perfect. The reason can be that the spinel structure in the resulting material is non-crystalline, e.g., the tetrahedral sites in the spinel structure are not 100% occupied and the number of mono-μ-oxo bridges between the Co atoms is lower than predicted. Additional insights into the structure of these materials can be obtained from the simulations of EXAFS spectra (Fig. S23†). In the simulation of the EXAFS spectrum of the catalyst after CV appears an additional Co–Co distance of

3.16 Å (Table S5†) which is not typical for the spinel structure. This distance suggests the presence of structural motifs of a third phase, for example, $Co_5(OH)_4(POH)_2$ or $Co(OH)_2$.

To verify the cooperative effect of different true active structures involved in OER and HER catalysis, we synthesized the individual components of active structure present in CoPn during OER (CoOOH, Co_3O_4, $Co(OH)_2$) and HER (Co_3O_4, Co and $Co(OH)_2$) and tested in a similar fashion to that of CoPn in 1 M aqueous KOH solution (see Experimental section). When compared, surprisingly, the CoPn exhibited much superior activity in both HER and OER, signifying the importance of the collective components of the active structures over a single constituent (Fig. S24 and S25†).

The excellent performance of CoPn as the bifunctional catalyst led us to construct a two-electrode system by employing NF supported CoPn as the anode and cathode. The overall water splitting reaches a current density of 10 mA cm^{-2} at only 1.62 V (Fig. S26†). Besides, excellent long-term stability of 25 h was established for CoPn/NF, representing it as one of the most competent catalytic systems for alkaline water electrolysis (Fig. S27†).

Conclusions

For the first time, we have demonstrated that cobalt phosphonate is a new class of highly active pre-catalysts for overall water splitting in alkaline media. Remarkably, it acts as a dual precursor for OER and HER: (i) under OER conditions, pristine cobalt phosphonate is transformed into layered Co oxides (CoCat) similar to crystalline CoO(OH) but with a lower degree of order to facilitate OER, while (ii) under HER conditions, metallic Co is produced as active species for H_2 production which is promoted by the presence of spinel Co_3O_4 and $Co(OH)_2$. The bifunctionality of the (pre)catalyst was further explored for overall water splitting that showed a very low cell voltage with high durability. Our investigation revealed new insights into the evolution and complex nature of interface structures to achieve highly efficient and durable overall water-splitting electrocatalysts, originating from the same metal-phosphorus-containing single-source precursor.

Conflicts of interest

There are no conflicts to declare.

Acknowledgements

This journal is © The Royal Society of Chemistry 2020

J. Mater. Chem. A, 2020, **8**, 2637–2643 | **2641**

Notes and references

1 I. Roger, M. A. Shipman and M. D. Symes, *Nat. Rev. Chem.*, 2017, **1**, 0003.

2 C. Panda, P. W. Menezes and M. Driess, *Angew. Chem., Int. Ed.*, 2018, **57**, 11130–11139.

3 F. Yu, L. Yu, I. K. Mishra, Y. Yu, Z. F. Ren and H. Q. Zhou, *Materials Today Physics*, 2018, **7**, 121–138.

4 (*a*) M.-I. Jamesh, Y. Kuang and X. Sun, *ChemCatChem*, 2019, **11**, 1550–1575; (*b*) Y. Zhu, H.-C. Chen, C.-S. Hsu, T.-S. Lin, C.-J. Chang, S.-C. Chang, L.-D. Tsai and H. M. Chen, *ACS Energy Lett.*, 2019, **4**, 987–994.

5 C. Panda, P. W. Menezes, M. Zheng, S. Orthmann and M. Driess, *ACS Energy Lett.*, 2019, **4**, 747–754.

6 N. T. Suen, S. F. Hung, Q. Quan, N. Zhang, Y. J. Xu and H. M. Chen, *Chem. Soc. Rev.*, 2017, **46**, 337–365.

7 H. Dau, C. Limberg, T. Reier, M. Risch, S. Roggan and P. Strasser, *ChemCatChem*, 2010, **2**, 724–761.

8 H. M. Xu, S. Q. Ci, Y. C. Ding, G. X. Wang and Z. H. Wen, *J. Mater. Chem. A*, 2019, **7**, 8006–8029.

9 T. Reier, M. Oezaslan and P. Strasser, *ACS Catal.*, 2012, **2**, 1765–1772.

10 Y. Jiao, Y. Zheng, M. T. Jaroniec and S. Z. Qiao, *Chem. Soc. Rev.*, 2015, **44**, 2060–2086.

11 B. You and Y. J. Sun, *Acc. Chem. Res.*, 2018, **1**, 1571–1580.

12 F. L. Lyu, Q. F. Wang, S. M. Choi and Y. D. Yin, *Small*, 2019, **15**, 1804201.

13 K. N. Dinh, Q. H. Liang, C. F. Du, J. Zhao, A. L. Y. Tok, H. Mao and Q. Y. Yan, *Nano Today*, 2019, **25**, 99–121.

14 X. H. Deng and H. Tuysuz, *ACS Catal.*, 2014, **4**, 3701–3714.

15 A. Bergmann, E. Martinez-Moreno, D. Teschner, P. Chernev, M. Gliech, J. F. de Araujo, T. Reier, H. Dau and P. Strasser, *Nat. Commun.*, 2015, **6**, 8625.

16 H. H. Zhong, C. A. Campos-Roldan, Y. Zhao, S. W. Zhang, Y. J. Feng and N. Alonso-Vante, *Catalysts*, 2018, **8**, 559.

17 P. W. Menezes, A. Indra, D. Gonzalez-Flores, N. R. Sahraie, I. Zaharieva, M. Schwarze, P. Strasser, H. Dau and M. Driess, *ACS Catal.*, 2015, **5**, 2017–2027.

18 M. W. Kanan and D. G. Nocera, *Science*, 2008, **321**, 1072–1075.

19 M. W. Kanan, Y. Surendranath and D. G. Nocera, *Chem. Soc. Rev.*, 2009, **38**, 109–114.

20 H. S. Ahn and T. D. Tilley, *Adv. Funct. Mater.*, 2013, **23**, 227–233.

21 D. Gonzalez-Flores, I. Sanchez, I. Zaharieva, K. Klingan, J. Heidkamp, P. Chernev, P. W. Menezes, M. Driess, H. Dau and M. L. Montero, *Angew. Chem., Int. Ed.*, 2015, **54**, 2472–2476.

22 Y. Y. Liu, H. T. Wang, D. C. Lin, C. Liu, P. C. Hsu, W. Liu, W. Chen and Y. Cui, *Energy Environ. Sci.*, 2015, **8**, 1719–1724.

23 J. Wang and H. C. Zengg, *ACS Appl. Mater. Interfaces*, 2018, **10**, 6288–6298.

24 P. W. Menezes, C. Panda, C. Walter, M. Schwarze and M. Driess, *Adv. Funct. Mater.*, 2019, 1808632.

25 F. Song, L. C. Bai, A. Moysiadou, S. Lee, C. Hu, L. Liardet and X. L. Hu, *J. Am. Chem. Soc.*, 2018, **140**, 7748–7759.

26 P. W. Menezes, A. Indra, V. Gutkin and M. Driess, *Chem. Commun.*, 2017, **53**, 8018–8021.

27 M. Risch, F. Ringleb, M. Kohlhoff, P. Bogdanoff, P. Chernev, I. Zaharieva and H. Dau, *Energy Environ. Sci.*, 2015, **8**, 661–674.

28 H. Kim, J. Park, I. Park, K. Jin, S. E. Jerng, S. H. Kim, K. T. Nam and K. Kang, *Nat. Commun.*, 2015, **6**, 8253.

29 L. Su, X. Z. Cui, T. He, L. M. Zeng, H. Tian, Y. L. Song, K. Qi and B. Y. Xia, *Chem. Sci.*, 2019, **10**, 2019–2024.

30 G. Q. Zhao, K. Rui, S. X. Dou and W. P. Sun, *Adv. Funct. Mater.*, 2018, **28**, 1803291.

31 P. W. Menezes, C. Panda, S. Garai, C. Walter, A. Guiet and M. Driess, *Angew. Chem., Int. Ed.*, 2018, **57**, 15237–15242.

32 J. Wang, H. X. Zhong, Z. L. Wang, F. L. Meng and X. B. Zhang, *ACS Nano*, 2016, **10**, 2342–2348.

33 Z. F. Dai, H. B. Geng, J. Wang, Y. B. Luo, B. Li, Y. Zong, J. Yang, Y. Y. Guo, Y. Zheng, X. Wang and Q. Y. Yan, *ACS Nano*, 2017, **11**, 11031–11040.

34 M. Caban-Acevedo, M. L. Stone, J. R. Schmidt, J. G. Thomas, Q. Ding, H. C. Chang, M. L. Tsai, J. H. He and S. Jin, *Nat. Mater.*, 2015, **14**, 1245–1251.

35 S. Cobo, J. Heidkamp, P. A. Jacques, J. Fize, V. Fourmond, L. Guetaz, B. Jousselme, V. Ivanova, H. Dau, S. Palacin, M. Fontecave and V. Artero, *Nat. Mater.*, 2012, **11**, 802–807.

36 P. W. Menezes, A. Indra, I. Zaharieva, C. Walter, S. Loos, S. Hoffmann, R. Schlogl, H. Dau and M. Driess, *Energy Environ. Sci.*, 2019, **12**, 988–999.

37 K. J. Gagnon, H. P. Perry and A. Clearfield, *Chem. Rev.*, 2012, **112**, 1034–1054.

38 T. H. Zhou, D. P. Wang, S. C. K. Goh, J. D. Hong, J. Y. Han, J. G. Mao and R. Xu, *Energy Environ. Sci.*, 2015, **8**, 526–534.

39 D. Shevchenko, M. F. Anderlund, A. Thapper and S. Styring, *Energy Environ. Sci.*, 2011, **4**, 1284–1287.

40 R. Zhang, P. A. Russo, A. G. Buzanich, T. Jeon and N. Pinna, *Adv. Funct. Mater.*, 2017, **27**, 1703158.

41 T. H. Zhou, Y. H. Du, D. P. Wang, S. M. Yin, W. G. Tu, Z. Chen, A. Borgna and R. Xu, *ACS Catal.*, 2017, **7**, 6000–6007.

42 Z. S. Cai, Y. Shi, S. S. Bao, Y. Shen, X. H. Xia and L. M. Zheng, *ACS Catal.*, 2018, **8**, 3895–3902.

43 Y. P. Zhu, T. Z. Ren and Z. Y. Yuan, *Nanoscale*, 2014, **6**, 11395–11402.

44 N. K. Chaudhari, H. Jin, B. Kim and K. Lee, *Nanoscale*, 2017, **9**, 12231–12247.

45 F. Lu, M. Zhou, Y. X. Zhou and X. H. Zeng, *Small*, 2017, **13**, 1701931.

46 Y. Wang, B. Kong, D. Y. Zhao, H. T. Wang and C. Selomulya, *Nano Today*, 2017, **15**, 26–55.

47 Q. Kang, L. Vernisse, R. C. Remsing, A. C. Thenuwara, S. L. Shumlas, I. G. McKendry, M. L. Klein, E. Borguet, M. J. Zdilla and D. R. Strongin, *J. Am. Chem. Soc.*, 2017, **139**, 1863–1870.

48 C. C. L. McCrory, S. H. Jung, J. C. Peters and T. F. Jaramillo, *J. Am. Chem. Soc.*, 2013, **135**, 16977–16987.

49 L. Yu, H. Q. Zhou, J. Y. Sun, F. Qin, F. Yu, J. M. Bao, Y. Yu, S. Chen and Z. F. Ren, *Energy Environ. Sci.*, 2017, **10**, 1820–1827.

2642 | *J. Mater. Chem. A*, 2020, **8**, 2637–2643

This journal is © The Royal Society of Chemistry 2020

50 A. Indra, P. W. Menezes, C. Das, D. Schmeisser and M. Driess, *Chem. Commun.*, 2017, **53**, 8641–8644.

51 Y. Surendranath, M. W. Kanan and D. G. Nocera, *J. Am. Chem. Soc.*, 2010, **132**, 16501–16509.

52 M. W. Kanan, J. Yano, Y. Surendranath, M. Dinca, V. K. Yachandra and D. G. Nocera, *J. Am. Chem. Soc.*, 2010, **132**, 13692–13701.

53 H. Guo, Q. Feng, J. Zhu, J. Xu, Q. Li, S. Liu, K. Xu, C. Zhang and T. Liu, *J. Mater. Chem. A*, 2019, **7**, 3664–3672.

54 H. Fei, Y. Yang, Z. Peng, G. Ruan, Q. Zhong, L. Li, E. L. G. Samuel and J. M. Tour, *ACS Appl. Mater. Interfaces*, 2015, **7**, 8083–8087.

This journal is © The Royal Society of Chemistry 2020

J. Mater. Chem. A, 2020, **8**, 2637–2643 | **2643**